

Phase coexistence and resistance relaxation kinetics in NdNiO₃ films below the metal-insulator transition temperature

Parushottam Majhi,^{1,*} Saikat Mitra,¹ Akriti Singh ² Barnali Ghosh,¹ V. R. Reddy,³ Surajit Saha,² and A. K. Raychaudhuri ^{4,†}

¹*Department of Condensed Matter and Materials Physics, S.N. Bose National Centre for Basic Sciences, JD Block, Sector III Salt Lake, Kolkata 700106, India*

²*Department of Physics, Indian Institute of Science Education and Research Bhopal, 1, Bhopal Bypass Rd, Bhauri, Bhopal 462066, India*

³*UGC-DAE Consortium for Scientific Research, University Campus, Khandwa Road, Indore 452001, India*

⁴*CSIR - Central Glass and Ceramic Research Institute, 196 Raja S.C. Mullick Road, Kolkata 700032, India*



(Received 2 June 2023; revised 31 July 2023; accepted 11 August 2023; published 21 August 2023)

Coexistence of electronically distinct phases below metal-insulator (MI) transition temperature (T_{MI}) in correlated oxides undergoing temperature-driven MI transition has been observed in a number of systems. One of the consequences of the coexisting phases is that the metastable high-temperature metallic phase transforms into the stable insulating phase with a finite relaxation time as the temperature is lowered below T_{MI} . We report an extensive investigation of the phase transformation (referred to as relaxation) using resistivity as a tool where the ramp-dependent hysteresis and isothermal annealing-induced resistance relaxation were studied in films of NdNiO₃ grown on three different crystalline substrates (LaAlO₃, SrTiO₃, and BaTiO₃/SrTiO₃) down to 10 K, well below the metal-insulator transition temperature. The resistance relaxation experiments were complemented with Raman spectroscopy and high-resolution x-ray diffraction done down to 5 K and reciprocal space mapping (RSM). Isothermal annealing experiment done to temperatures $< T_{MI}$ shows that the average relaxation time (τ) decreases on cooling. This can arise from a temperature-dependent barrier to relaxation, where the barrier reduces continuously on cooling down to a temperature, referred to as T^* . T^* has been interpreted as a likely limit of supercooling so that the relaxation time $\rightarrow 0$ at this temperature. The resistance relaxation data were linked to x-ray diffraction and Raman spectroscopy data done to temperatures well below T_{MI} , in order to have a structural basis for the coexisting phases and their likely participation in the relaxation process. The experiments (both hysteresis and isothermal annealing) were analyzed by Monte Carlo simulation based on a minimal set of parameters, namely, a temperature T^* and an energy scale of transformation E^* , which themselves had a temperature dependence. The parameters used in the simulation and other experimentally observed quantities like the width and height of hysteresis were found to be correlated with certain structural parameters, in particular, the residual in-plane strain and the crystallite grain size that determine the size range in these films.

DOI: [10.1103/PhysRevB.108.064103](https://doi.org/10.1103/PhysRevB.108.064103)

I. INTRODUCTION

Metal-insulator transition (MIT) as it happens in a correlated system is a fascinating phenomenon. This phenomenon has been studied in correlated oxides like V₂O₃ [1], VO₂ [2], NdNiO₃ [3–5], PrNiO₃ [6] for example, where a temperature-driven MIT occurs on cooling from a high-temperature metallic phase to a low-temperature insulating phase. The transition is often first order with symmetry change at the transition and is accompanied by hysteresis. Studies on rare-earth nickelates like NdNiO₃ have attracted current attentions owing to likelihood of multiferroic behavior in the insulating state due to breakdown of inversion symmetry [7,8] and also observation of superconductivity in a related Ruddlesden–Popper phase Nd_{0.8}Sr_{0.2}NiO₂ [9]. Recent experiments and models suggest existence of charge disproportionation as a

likely origin of the MIT [7,10]. These developments necessitate an intensive investigation on phase existence and related phenomena of relaxation and hysteresis.

The occurrence of phase coexistence near the MIT and the associated physics have been investigated for some time in different oxide systems. In recent years the issues of the electronic phase separation and phase coexistence have attracted renewed attentions, due to sustained theoretical developments as well as due to innovative use of different types of direct imaging techniques like scanning tunneling microscopy and spectroscopy (STM/STS) with near-atomic level resolution [11] and spatially resolved infrared imaging including near-field imaging with spatial resolution ≈ 25 nm [12–14]. There are a number of important outcomes from these experiments. For instance, it has been established that the coexisting phases indeed have different electronic signatures and their density of states near the Fermi level [$N(E_F)$] show clear signatures of both correlated metallic and insulating phases. It has been observed that there is persistence of the high-temperature metallicity within the insulating phase

*parushottam.physics@gmail.com

†Corresponding author: arupraychaudhuri4217@googlemail.com

below the MIT [11,14]. The scale of phase separation is in the nanoscopic to mesoscopic regime. Also, the relative volume fractions of the coexistence phases vary with temperature. This leads to an aspect of percolation that determines the temperature dependence of resistivity and the transition temperature as determined from resistivity data. However, the underlying transition is first-order phase transition that involves a change in symmetry. For NdNiO₃ the MI transition involves a change from high-temperature orthorhombic phase with *Pnma* symmetry to the low-temperature monoclinic phase with *P2_{1/n}* symmetry as observed in electron, x-ray, and neutron diffraction as well as Raman spectroscopy [15–17].

A particular mention be made of the recent near-field imaging of the MIT in 300 nm oriented V₂O₃ film [12]. It has been observed that the underlying structural transition at MIT directs the correlation-driven electronic transition. Both the structural as well as the electronic correlation lengths grow from nanoscopic scales to mesoscopic scale (fraction of a micron to a micron), close to the transition. We propose to investigate in this paper a closely related issue. How does the morphology and the residual strain of a film grown on a substrate affect the length scales mentioned above. This in turn may affect the kinetics of relaxation below the metal-insulator transition temperature (T_{MI}) as they can modulate the energy barrier for phase transformation.

In addition to direct imaging methods as mentioned before, experiments of “bulk” nature, that probe the kinetics and dynamics associated with the coexisting phases, can observe clear signatures of the nanoscopic phase separation. As an example, appearance of large thermal noise (much larger than the anticipated Nyquist noise) [18] near the T_{MI} has been traced to nanoscopic phase separation. The phase separation also leads to onset of slow electronic relaxation, which can give rise to electronic Griffiths phase as observed in polymeric systems [19] and also in oxides [20].

In the phase coexistence region below T_{MI} , the persistence of the high-temperature metallic phase in the matrix of the low-temperature insulating phase creates a metastable condition [6], because the high-temperature metallic phase can relax to the equilibrium insulating phase with a finite relaxation time. Cooling further below T_{MI} will change the relative volume fractions of the two phases, but there is a likelihood of presence of a small but finite volume fraction of the high- T phase well below the transition temperature. The consequence of this will be hysteretic cooling and heating curves at a finite rate of cooling and heating. The presence of the metastable high-temperature phase would also lead to an evolving time-dependent volume fraction when an isothermal anneal is done at a temperature below T_{MI} after cooling at a given rate. The discussion above has been done in the general context of a temperature-driven MIT, which is expected to have a broad validity in all such systems undergoing MIT. However, details of each material undergoing MIT would have contributions that are materials specific.

In NdNiO₃ there are specific issues of phase coexistence and the phase transformation like symmetry of the two phases and also the likelihood that the low-temperature phase can have charge and bond disproportionation as opposed to uniformly trivalent Ni³⁺ in the high-temperature metallic phase

[10]. In addition, there are recent reports that Ruddlesden–Popper faults in NdNiO₃ thin films can significantly affect the electronic transport as well as the coexisting phases [21]. The extent of phase separation as well as the existence of Ruddlesden–Popper faults depend on the strain (or residual strain in case of strain relaxation) in the film that can be controlled by growing them on different substrates. In this article we report an extensive investigation of kinetics of relaxation in NdNiO₃ films grown on different crystalline substrates, which shows a clear MIT [11,20] and phase coexistence below T_{MI} .

It has been established in previous investigations that the resistance relaxation method [22] is a viable method to study relaxation kinetics of coexisting phases because the coexisting phases have different resistivities (ρ) or conductivities (σ). The conductivity of a solid with coexisting phases is like that of a composite medium where the volume fractions of the two phases determine the resulting conductivity and this can be quantified by an effective medium theory [23,24]. This changing relative volume fraction on isothermal annealing below the T_{MI} will show up as a time-dependent conductivity (or resistivity) of the solid undergoing an isothermal annealing below T_{MI} .

Presence of the metastable metallic phase below T_{MI} also gives rise to hysteresis when the temperature is cycled above and below the T_{MI} with a finite rate of heating and cooling ($\frac{dT}{dt}$) due to finite relaxation time (τ) of the metallic phase. When the solid undergoes cooling/heating at a finite rate, if the rate $\frac{dT}{dt}$ is too fast compared to the relaxation rate ($\frac{1}{\tau}$), then there will be unrelaxed high-temperature phase during cooling coexisting with the equilibrium phase. On heating, the growth of the volume fraction of the metallic phase, will follow a different path due to the presence of the unrelaxed phase. This will give rise to a rate-dependent hysteretic resistivity vs T curve. Quantitative analysis of resistivity data for both the isothermal annealing and rate-dependent hysteresis will identify the relevant parameters that control the relaxation process. In this investigation we have carried out a physical model-dependent Monte Carlo simulation with a set of parameters that can quantitatively describe both the hysteresis as well as isothermal kinetics

The phase coexistence and relaxation below T_{MI} have been studied in NdNiO₃ films grown on three different substrates (LaAlO₃, SrTiO₃, and BaTiO₃/SrTiO₃) that result in different structural features (as revealed through temperature-dependent x-ray diffraction, XRD), and morphology (as revealed through atomic force microscopy), and residual strain (as revealed through reciprocal space mapping). The phase transition at the T_{MI} shows a clear signature of change in symmetry as noted from Raman spectroscopy done to 5 K on films of NdNiO₃/LaAlO₃, which also shows signature of phase coexistence. These factors, as we show below, clearly affect the relaxation kinetics. This is likely an evidence that the phase coexistence in such MIT can indeed be controlled by structural factors.

It is noted that resistance relaxation experiments under isothermal annealing below T_{MI} have been carried out on bulk pellets of PrNiO₃ [6] and NdNiO₃ [22], which indicates the existence of slow kinetics. However, these experiments did not

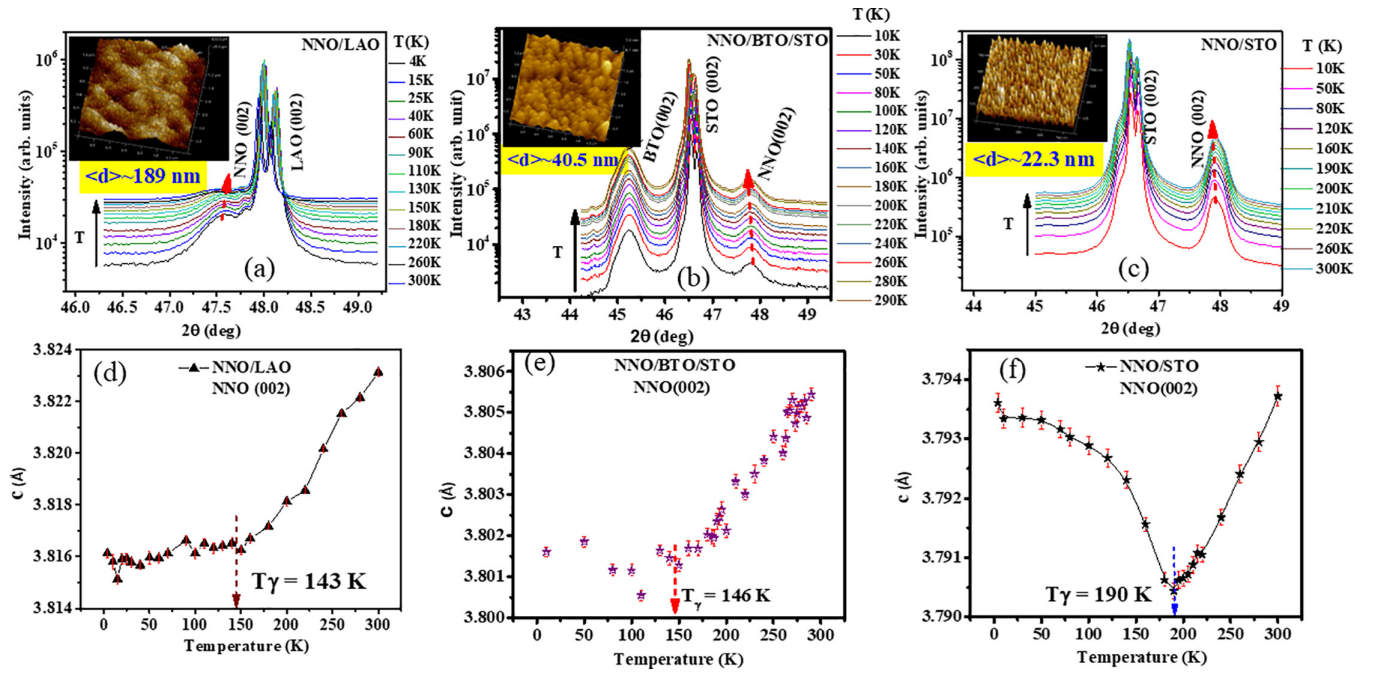


FIG. 1. Temperature-dependent XRD data of NdNiO₃ films grown on (a) LAO, (b) BTO/STO, and (c) STO substrates. Inset: AFM images of the films. Average grain size ($\langle d \rangle$) for each film is shown at bottom. The variation of the out-of-plane lattice constant c with T for (d) NNO/LAO, (e) NNO/BTO/STO, and (f) NNO/STO films indicating the structural evolution. The temperature T_γ marks the break in slope of variation of c with T , which arises from structural transition.

have any structural characterizations or Raman spectroscopy data that allow one to connect the structural and associated parameters with the relaxation kinetics.

II. EXPERIMENTAL DETAILS

The NdNiO₃ films (thickness ≈ 27 nm) were grown by pulse laser deposition (PLD) using KrF laser ($\lambda = 248$ nm) on three different single crystalline substrates namely LaAlO₃(LAO), SrTiO₃(STO), and on a BaTiO₃ layer of thickness ≈ 110 nm grown on SrTiO₃ substrate and referred to as BaTiO₃/SrTiO₃ (BTO/STO). All the substrates used are (001) oriented. The films grown on the three substrates differ in the residual strain in them as well as the grain morphology. A well-characterized NdNiO₃ pellet has been used as the target material for the ablation. All the films on the three substrates were grown in the same growth run to ensure that the films are grown in identical ambience with same laser fluence. The depositions have been carried out at temperature 675 °C with base chamber pressure 10^{-6} mbar, and oxygen pressure of 0.2 mbar during deposition. After deposition all the films were subjected to a postgrowth oxygen anneal in the growth chamber for 1 hr at 1-atm oxygen pressure to maintain its desired stoichiometry. The details of the film deposition process are given in previous publications from our group [11].

For the structural characterization at room temperature, we used x-ray diffraction (XRD) and atomic force microscopy (AFM). In addition, XRD data were also taken as a function of temperature from 300 K down to 10 K.

We have also done investigation of Raman spectra on a film of NdNiO₃/LaAlO₃ over the temperature range from

5 K to 200 K. Though Raman spectra has been reported on polycrystalline and textured film as well as recently on single crystals [8], the Raman data was necessitated to establish the existence of the underlying phase transition because a much thinner film has been used here and also as we will see below we could establish a likely link of coexisting phases and the Raman lines with definite vibrational modes.

The Raman measurements were performed in the backscattering geometry using the LabRAM HR Evolution Raman Spectrometer equipped with a Peltier cooled charge-coupled device (CCD) detector. A laser excitation of wavelength 532 nm and power of nearly 2 mW was focused using a 100 \times objective (numerical aperture = 0.8) to a spot size less than a micron on the sample/film. The spectrometer was optically coupled to a closed-cycle helium cryostat (attoDRY1000) to perform the temperature-dependent Raman measurements from 5 K to 200 K [25].

The electrical resistivity measurements have been carried out down to 10 K using a low-temperature cryocooler system connected to a custom-made automated measurement unit, which is able to record temperature and time-dependent resistivity data and also can control the rate of cooling and heating. We have covered a range of controlled uniform heating/cooling ramp rate starting from 0.2 K/min upto 15 K/min. For the low-temperature kinetics measurement at isothermal anneal, samples were cooled to the desired anneal temperature T_a ($< T_{MI}$), where it was held for at least 2 hrs. The duration of the isothermal anneal was found to cover more than 5–15 time constants of relaxation even in the slowest process. After completion of the heating cycle we have waited for 1 hr at 300 K ($\gg T_{MI}$) to erase the previous cooling memory before start of the next cooling cycle.

TABLE I. Structural parameters of the films.

Sample	$\langle d \rangle$ (nm)	R (%)	ϵ_{\parallel} (%)	T_{γ} (K)
NNO/LAO	189 ± 3	0.99	-0.89	143
NNO/BTO/STO	40.5 ± 0.5	1.1	-0.59	146
NNO/STO	22.3 ± 0.3	0.96	0.094	190

$\langle d \rangle$, average grain size; R, relaxation; ϵ_{\parallel} , in-plane residual strain; T_{γ} , monoclinic to orthorhombic transition temperature.

III. RESULTS

A. Structural and Raman spectroscopy data

1. Characterization of the films

Figures 1(a)–1(c) shows the XRD data of the NNO films grown on LAO, STO, and BTO/STO substrates taken over the temperature range from 300 K down to ≤ 10 K. The XRD data show highly oriented film growth along the (001) crystallographic direction, here only the (002) peaks are shown along with those of the substrates. The full 2θ scale XRD data of the films are given in Supplemental Material (SM) [26] as Fig. S1.

The NdNiO₃ films are strongly textured along the (001) axis of the substrates. However, finite mismatches of lattice constants of the films with those of the substrates lead to strain relaxation with creation of dislocations and a residual in-plane strain (ϵ_{\parallel}) as established through reciprocal space mapping (RSM). (The RSM data are given in SM [26] as Fig. S2.) The in-plane and out-of-plane residual strains have been estimated using the formulas $\epsilon_{\parallel} = \frac{a_{\text{film}} - a_{\text{film}}^R}{a_{\text{substrate}}}$ and $\epsilon_{\perp} = \frac{c_{\text{film}} - c_{\text{film}}^R}{c_{\text{substrate}}}$ from RSM data. The relaxation parameter R is estimated from $R = \frac{a_{\text{film}} - a_{\text{substrate}}}{a_{\text{film}}^R - a_{\text{substrate}}}$ and placed in Table I, a and c being the in-plane and out-of-plane lattice constants, respectively. Subscripts “film” and “substrate” refer to film and the substrate, respectively. The superscript R refers to the fully relaxed film. These structural aspects are expected to have an important role in the kinetics of phase transformation below T_{MI} as discussed later on.

In insets of Figs. 1(a)–1(c) show the AFM images of the films, which show their compact granular morphologies and the average grain size depends on the substrate on which the film is grown. The average grain size as obtained from grain size distribution are shown in Table I.

2. Temperature-dependent evolution of lattice constants

We have used temperature-dependent XRD to investigate the evolution of the lattice constants of the films as a function of temperature. Data were taken during heating cycle with temperature stabilized at each point to within ± 5 mK for at least 15 mins. Shift of the (002) peak positions of the NdNiO₃ film as well as that of the substrate with T are shown in Figs. 1(d)–1(f) for NNO/LAO, NNO/STO, and NNO/BTO/STO films respectively. The out-of-plane lattice constants c were obtained from the peak positions.

The MI transition in NdNiO₃ is accompanied by a change in symmetry from low-temperature monoclinic to high-temperature orthorhombic phase when warmed up through T_{MI} [27]. The variation of the lattice constant (c) with T are shown in Figs. 1(d)–1(f). Major slope changes have been

observed at a temperature marked as T_{γ} ($\approx T_{MI}$), which arise from this change in symmetry. The variation of c with T for the films NNO/LAO and NNO/BTO/STO are qualitatively similar, but for the NNO/STO film there is a sharp up turn of c below T_{γ} as marked.

The NNO/STO film has finite residual in-plane tensile strain ϵ_{\parallel} (see Table I) that stabilizes the insulating phase leading to the highest T_{MI} among the three films. (A comparison with bulk data are given in SM [26].) The tensile strain increases the distortion of the NiO₆ octahedron and this stabilizes the low-temperature monoclinic phase with $P2_{1/n}$ symmetry of the insulating phase. Thus, a tensile strain stabilizes the insulating phase and enhances the metal-insulator transition temperature T_{MI} . The NNO/STO film with largest built-in residual tensile strain thus has the highest T_{MI} . The other two films have residual in-plane compressive strains. The magnitude of the strain is somewhat higher for the NNO/LAO film in comparison to that in NNO/BTO/STO film, leading to stabilization of the high-temperature metallic phase down to lower temperature and a comparatively suppressed T_{MI} .

The relaxation (transformation) of the high- T orthorhombic metallic phase below T_{MI} to the low-temperature monoclinic insulating phase would involve a local symmetry change and accommodation of the local crystal structure and the strain. (Note: The orthorhombic phase has $Pnma$ symmetry and the low-temperature monoclinic phase with $P2_{1/n}$ symmetry. Usually elimination of mirror symmetry plane from the $Pnma$ symmetry leads to $P2_{1/n}$ symmetry.) It is thus expected that the stability (or lack of it) of the minority metallic phase in the insulating matrix below T_{MI} would determine at least partially the kinetics of the relaxation.

3. Temperature-dependent Raman spectra

The Raman spectra were recorded on the NdNiO₃/LaAlO₃ film over the temperature range from 5 K to 200 K. Figure 2(a) represents the spectra from the sample (film and substrate) for the frequency range 50 cm⁻¹ to 550 cm⁻¹ at some representative temperatures that contain the MIT. Due to strong interference from substrate peaks (given small film thickness) we could not obtain well-resolved peaks from NdNiO₃ film grown on the other two substrates.

A coloured contour plot of the Raman data are shown in Fig. 2(b) and the prominent line positions as a function of temperature are shown in Fig. 2(c). The Raman data shown here broadly agrees with that for single crystals as well as from films albeit with shift in peak positions [8,16,17]. The symmetry modes associated with the Raman spectra are given in SM [26] in Table 1.

The following are some of the important observations from the Raman spectroscopy. (a) For $T < T_{MI}$ there are a few modes that cease to exist beyond the T_{MI} , signifying an occurrence of change in symmetry at the transition [16,17]. (b) Some modes extend over the entire temperature range under study, which might be the allowed modes for both symmetries. (c) Importantly, the modes in the vicinity of 300 cm⁻¹ (p12 marked in figure) as well as 255 cm⁻¹ (p8) carry clear signatures of phase coexistence for $T \leq T_{MI}$. T_{MI} as determined from the resistive transition data is marked in the Fig. 2(c).

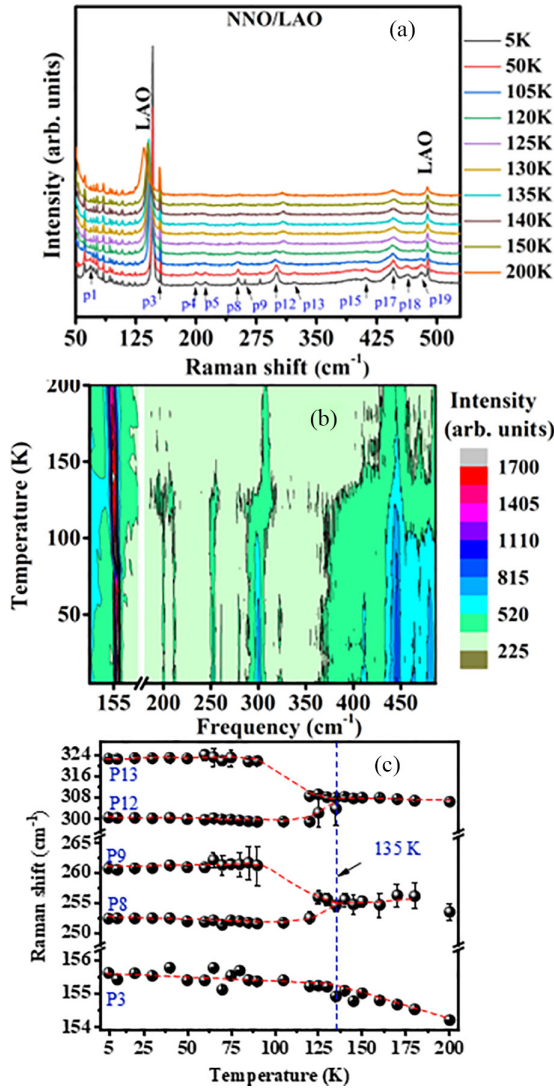


FIG. 2. (a) The Raman spectra for NNO/LAO film at few representative temperatures. (b) A colored contour plot of Raman data showing the evolution of Raman mode with both frequency and temperature. (c) The prominent line positions as a function of temperature are shown. The vertical line marked as MIT refers to T_{MI} obtained from resistivity data.

The phase coexistence is visible in the Raman spectra in that temperature range $\frac{T}{\langle T_{MI} \rangle} \geq 0.8$. It may happen that the Raman signature of the high-temperature mode may extend below this temperature as well due to persistence of the high-temperature phase but due to its progressively small fraction (which we will show below reaches $\ll 10^{-4}$ for $\frac{T}{\langle T_{MI} \rangle} \leq 0.8$) the line may not have enough intensity to be detectable. (d) The temperature at which the symmetry changes (on heating) as recorded from the Raman data is lower than the transition temperature recorded by the resistive transition (to be shown below). Similar observation was reported in previous publication [17]. The difference is likely due to the local nature of the Raman spectroscopy and the percolative nature associated with the resistive transition (which will be quantified in subsequent sections).

B. Hysteretic resistivity data for different ramp rates

One of the signatures of the metastability and relaxation at $T < T_{MI}$ is the hysteresis that separates out the path of the resistivities $[\rho(T)]$, which it traverses from 300 K to 10 K (during cooling) from that traversed from 10 K to 300 K (during heating). The hysteresis has been measured with different controlled ramp rates ($\frac{dT}{dt}$) of heating and cooling starting from 0.2 K/min to 15 K/min (Fig. 3). The evolution of the hysteresis curves varied with ramp rate is linked to the kinetics of relaxation of the high-temperature metallic phase below T_{MI} . Insight into this link has been explored later on through Monte Carlo simulation.

With enhancement of the ramp rate the T_{MI} during cooling moves to lower temperature and that during heating moves out to higher temperature, which enhances the width of the hysteresis curves. This also increases the separation of the resistivities during heating and cooling thus enhancing the height of the hysteresis curve. We have quantified two parameters of hysteresis curve, namely, scaled height of hysteresis, i.e., $\xi(T = \langle T_{MI} \rangle)$ at average phase transition temperature, $\langle T_{MI} \rangle$ and width of hysteresis, i.e., ΔT_{MI} . These parameters are defined below:

$$\Delta T_{MI} = T_{MI,H} - T_{MI,C}, \quad (1)$$

$$\langle T_{MI} \rangle = \frac{T_{MI,H} + T_{MI,C}}{2}, \quad (2)$$

$$\langle \rho(T) \rangle = \frac{\rho_H(T) + \rho_C(T)}{2},$$

$$\Delta \rho(T = \langle T_{MI} \rangle) = \rho_H(T) - \rho_C(T),$$

$$\xi(T = \langle T_{MI} \rangle) = \frac{\Delta \rho(T = \langle T_{MI} \rangle)}{\langle \rho(T = \langle T_{MI} \rangle) \rangle}. \quad (3)$$

The H and C in subscripts refer to heating and cooling cycles respectively. $\langle T_{MI} \rangle$ and $\langle \rho(T) \rangle$ are the average transition temperature and average resistivity at a given T respectively. Both the parameters, ΔT_{MI} and $\xi(T = \langle T_{MI} \rangle)$, are enhanced with increasing ramp rate as shown in Figs. 4(b) and 4(c). There is a power-law dependence of both the parameters with ramp rate. [Note: Figures 4(b) and 4(c) are plotted in log-log scale, barring that of NNO/LAO in Fig. 4(b), to bring out this power-law dependence.] However, there is enhanced dependence on $\frac{dT}{dt}$ for ramp rate > 5 K/min. This is also observed in Fig. 4(a) for T_{MI} . This would imply additional factors (e.g., partial loss of thermal equilibrium) that enhance the area of the hysteresis curves. This departure being small has not been explored further.

The noticeable change in the value of T_{MI} is observed for NNO/LAO whereas lesser change reported for NNO/STO. The moderate change in hysteresis area and T_{MI} observed for NNO/BTO/STO film. Width of hysteresis ΔT_{MI} as well as the scaled height ξ vary in the films in the order of NNO/LAO $>$ NNO/BTO/STO $>$ NNO/STO. There is another aspect, which is worth noting in the data taken on different films. The hysteresis curves do not close at low-temperature in the films grown on STO and BTO/STO. This aspect, as discussed in the next subsection is linked to resistivity relaxation at $T < T_{MI}$.

The experimental data show that shift of T_{MI} and area of hysteresis depend significantly on the substrate on which the

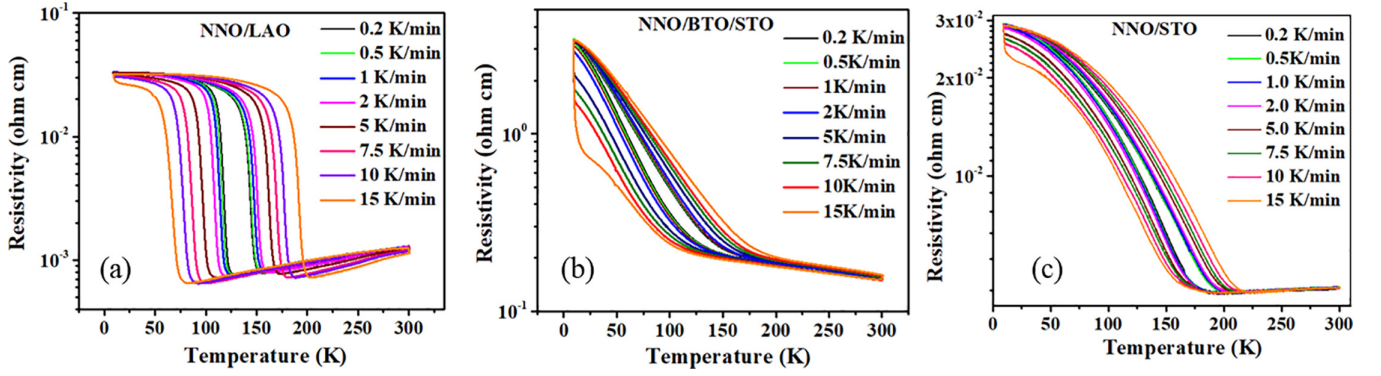


FIG. 3. The ramp rate-dependent resistivity data during cooling and heating in the temperature range 10 K to 300 K of (a) NNO/LAO, (b) NNO/BTO/STO, and (c) NNO/STO films. The ramp rate for cooling and heating were varied between 0.2 K/min to 15 K/min.

film is grown (Table II). For instance, for the cooling/heating rate of 5 K/min the parameters ΔT_{MI} and ξ are respectively 60 K and 1.874 for the film NNO/LAO. For NNO/STO film the same parameters reduce to 18 K and 0.034 respectively. We note that the hysteresis width recorded by the resistivity data on the NdNiO₃/LaAlO₃ film at low-ramp rate (≈ 1 K/min) agrees well with the phase coexistence range observed in the Raman data on the film [see Fig. 2(c)] as well as that in single crystal [8].

C. Isothermal annealing below T_{MI} and the kinetics of resistivity relaxation:

The kinetics of relaxation of the metastable high temperature metallic phase to the low temperature equilibrium insulating phase below T_{MI} during cooling cycle is an important part of this study. This is directly linked to the observed hysteresis observed in the resistivity data [Figs. 3(a)–3(c)]. In order to unambiguously evaluate the relaxation time and its temperature dependence, the time-dependent resistivity data have been collected in isothermal condition by fixing the temperature at various annealing temperatures $T = T_a < T_{MI}$ in the cooling cycle following a uniform rate of cooling at 5 K/min starting from room temperature. For all the cases we applied an isothermal anneal time $t_a = 2$ hrs, which is much longer than the average relaxation time $\langle \tau \rangle$. Following an anneal at a given T_a , the sample was heated back up to

room temperature and annealed at room temperature for a time $t_{RT} = 1$ hr. This is followed by the next cooling cycle. The cyclic resistivity curves for cooling and subsequent heating cycles for isothermal anneals at different temperature (T_a) for all the three samples are shown in Figs. 5(a)–5(c). Figures 5(d)–5(f) show the time-dependent relaxation of resistances during isothermal annealing at some representative T_a s. For long annealing time ($t_a \rightarrow \infty$) the resistivity reaches the equilibrium value corresponding to that temperature, which is designated as ρ_∞ . The initial starting value of the resistivity at the start of the annealing $t_a \rightarrow 0$ is designated as ρ_0 . The time-dependent resistivity relaxation curves [as shown in Figs. 5(d)–5(f)] were fitted to stretched exponential function shown below:

$$\rho = \rho_\infty - \rho_1 \exp \left[- \left(\frac{t}{\tau} \right)^\beta \right], \quad (4)$$

$\rho_1(t) = \rho_\infty - \rho_0$ the relaxing part of the resistance. By fitting Eq. (4) to the resistivity relaxation data, the exponent β and relaxation time τ are obtained. From the τ , we obtained the mean relaxation time of relaxation $\langle \tau \rangle$ given as $\langle \tau \rangle = \frac{\tau}{\beta} \Gamma(\frac{1}{\beta})$; $\Gamma(\frac{1}{\beta})$ being the Gamma function [28].

The deviation of β from 1 shows non-Debye nature of relaxation. The stretched exponential relaxation or the non-Debye relaxation can arise from a distribution of relaxation times of the relaxing entities or due to hierarchical relaxation

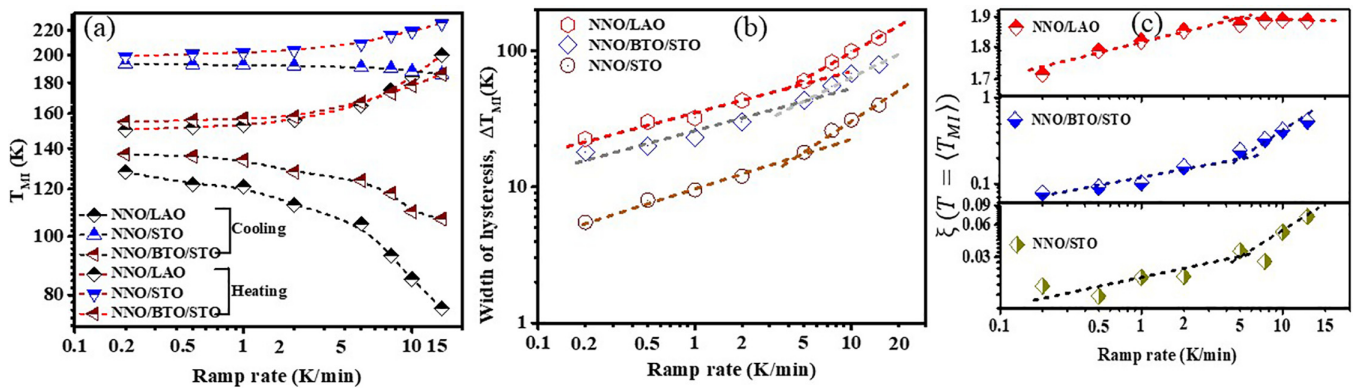


FIG. 4. The variations (a) T_{MI} , (b) width of hysteresis (ΔT_{MI}), and (c) scaled height of hysteresis (ξ) with ramp rate for NNO/LAO, NNO/BTO/STO, and NNO/STO films. Data obtained from ramp rate-dependent hysteresis data in Fig. 2.

TABLE II. Parameters linked to hysteresis at ramp rate 5 K/min.

Sample	$T_{MI,H}$ (K)	$T_{MI,C}$ (K)	$\langle T_{MI} \rangle$ (K)	ΔT_{MI} (K)	$\xi(T = \langle T_{MI} \rangle)$	ρ (ohm cm) at 300 K	ρ (ohm cm) at 10 K
NNO/LAO	165	105	135.0	60	1.874	1.3×10^{-3}	3.3×10^{-2}
NNO/BTO/STO	167	124	145.5	43	0.245	1.5×10^{-1}	3.3×10^0
NNO/STO	209	191	200.0	18	0.034	4.6×10^{-3}	2.9×10^{-2}

[29]. Plot β with scaled temperature $\frac{T_a}{T_{MI}}$ for the three films are shown in Fig. 6(a). (In Fig. S3 within SM [26], detailed data on variations of the parameters β and the ratio $\delta\rho_{\text{relax}} = \frac{\rho_l}{\rho_\infty}$ with the annealing temperature are shown for all the three films.) β lies between 1 and 0.75 for all the films. The three films show somewhat quantitatively different β both in their values and dependence on temperatures as derived from their dependence on T_a .

The deviation of β from 1 can arise from a combination of two factors namely distribution in relaxation times as well as hierarchical relaxation [29]. Close to T_{MI} , the volume fraction of the high- T metallic phase is high and there will be a size distribution. Since the two phases have different crystallographic symmetry, transformation of the phase would need lattice accommodation. It is expected that size distribution would imply a distribution of the relaxation time τ giving rise to stretched exponential behavior with $\beta < 1$. In the

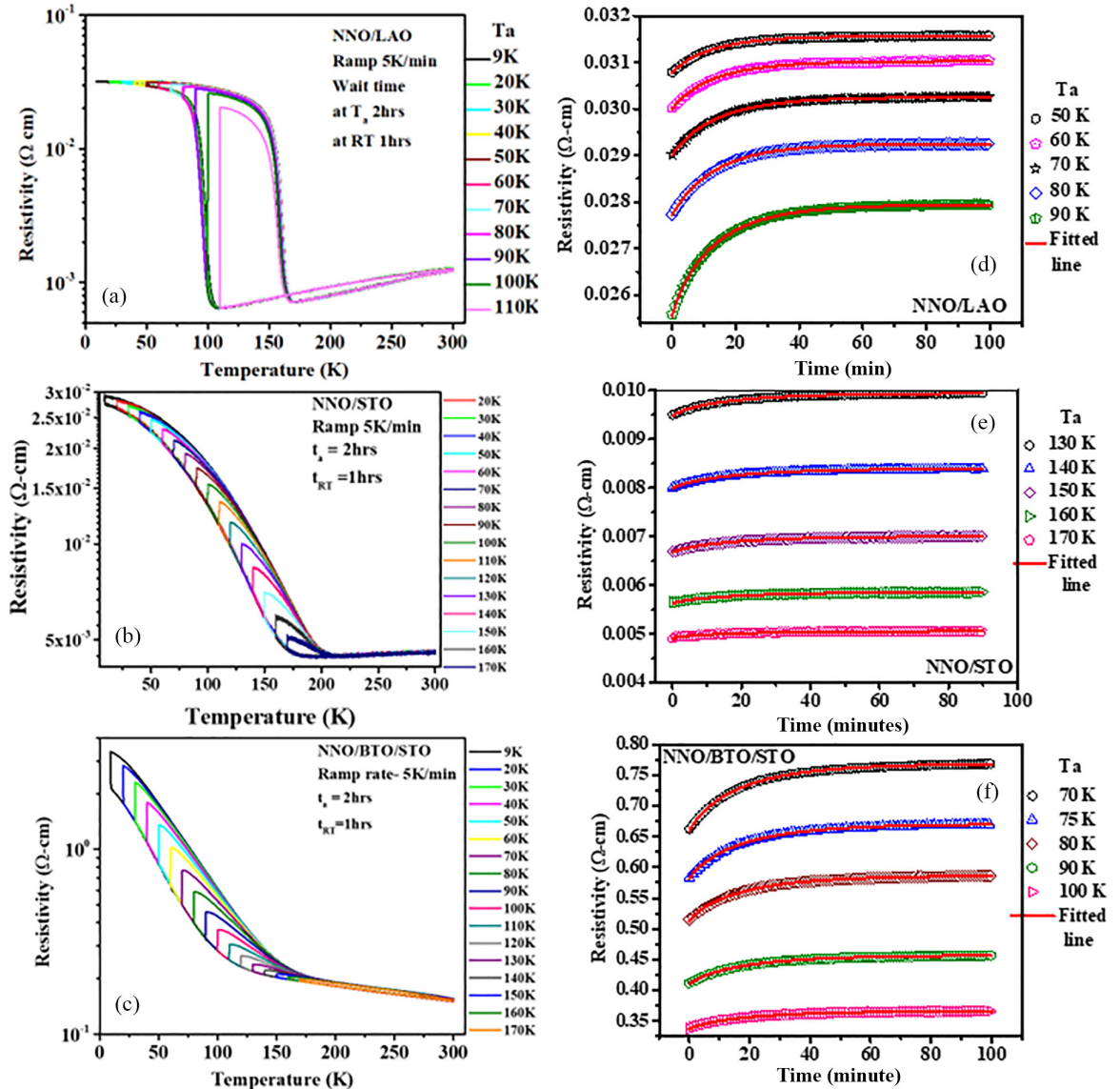


FIG. 5. Hysteresis with isothermal annealing at several T_a for (a) NNO/LAO, (b) NNO/STO, and (c) NNO/BTO/STO films. The resistivity relaxation curves under isothermal annealing for few representative T_a for (d) NNO/LAO, (e) NNO/STO, and (f) NNO/BTO/STO films. The lines through the data are fits to the stretched exponential relation.

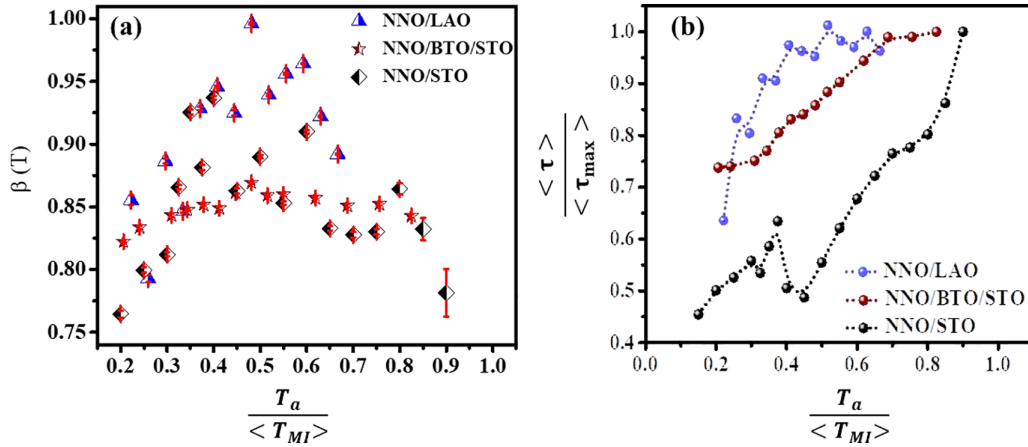


FIG. 6. (a) The variation of β with scaled $\frac{T_a}{\langle T_{MI} \rangle}$ for the three samples NNO/LAO, NNO/BTO/STO, and NNO/STO. (b) The variation of scaled $\frac{\langle \tau \rangle}{\langle \tau_{\max} \rangle}$ with scaled $\frac{T_a}{\langle T_{MI} \rangle}$ for the three samples NNO/LAO, NNO/BTO/STO, and NNO/STO.

low-temperature range end where the annealing temperature is $\ll T_{MI}$, the high-temperature phase will be sparse with smaller sizes distributed in the majority insulating phase. In this case, the relaxation of phase would include sequential relaxation in the majority phase to accommodate the relaxation in the minority phase. This would imply a hierarchical relaxation with non-Debye character and lowering of β .

D. Dependence of relaxation time $\langle \tau \rangle$ on temperature

The evolution of the average relaxation time $\langle \tau \rangle$ as a function of annealing temperature T_a has been obtained from the isothermal relaxation data. This gives the temperature dependence of $\langle \tau \rangle$. In Fig. S4 within SM [26], we plot the average relaxation time ($\langle \tau \rangle$) as a function of T_a for all the samples. The value of $\langle \tau \rangle$ as well as its detailed dependence on T_a depends on the films. However, the scale of $\langle \tau \rangle$ is in the range of tens to few tens of minutes in all the films. Also for all the films, the data show a clear trend. $\langle \tau \rangle$ shows a general drop as the temperature is reduced. The later observation, in particular, has important consequences as discussed in the next section.

To compare the temperature dependence of relaxation times as observed in the three films, we present in Fig. 6(b) a scaled graph of $\frac{\langle \tau \rangle}{\langle \tau_{\max} \rangle}$ vs $\frac{T_a}{\langle T_{MI} \rangle}$. $\langle \tau_{\max} \rangle$ is the maximum value of the average relaxation time for a given film as it happens when $T_a \rightarrow \langle T_{MI} \rangle$. It can be seen from Fig. 6(b) that there are two distinct regions in the temperature dependence of the relaxation process. For $\frac{T_a}{\langle T_{MI} \rangle} \geq 0.7$, the relaxation rate has a shallow temperature dependence for NNO/LAO and NNO/BTO/STO while it decreases for NNO/STO. For $0.7 > \frac{T_a}{\langle T_{MI} \rangle} > 0.4$, for all the films the relaxation time decreases monotonously. At $\frac{T_a}{\langle T_{MI} \rangle} \approx 0.4$ there is a break in slope and at lower temperature it decreases further albeit with different slopes. For the film NNO/STO there is a local small maxima around $\frac{T_a}{\langle T_{MI} \rangle} \approx 0.4$, pointing to a slowing down of the relaxation process over a small temperature region.

Figure 6(b) also shows that for $\frac{T_a}{\langle T_{MI} \rangle} \leq 0.4$, there is a finite relaxation time associated with the relaxation of the high-temperature metallic phase. This points to some degree of

persistence of the high-temperature phase well below $\langle T_{MI} \rangle$, even with a small volume fraction.

At this point a broad qualitative correlation with the temperature dependence of the lattice constant can be made to rationalize the observed variations of $\frac{\langle \tau \rangle}{\langle \tau_{\max} \rangle}$ with temperature. One of the factors that would determine the ease of transformation and hence the relaxation time is the stability of the metallic phase for $T < T_{MI}$. In NNO/STO, the residual strain being tensile (see Table I), this makes the metallic phase less stable. This makes the relaxation just below T_{MI} to drop. Below T_{MI} , the out-of-plane c enhances on cooling leading to decrease of the in-plane lattice constant thus decreasing the tensile strain to a degree. It can be seen from Fig. 1(f) that the enhancement of c is rapid in the temperature range $T_{MI} \geq 0.4$. The modest local enhancement of the relaxation time in this temperature region may thus be related to this effect. For the other two films, the residual strain being compressive in nature, the metallic phase will have relatively higher stability leading to longer relaxation time (larger $\langle \tau \rangle$) and there is temperature independence of the relaxation time for $\frac{T_a}{\langle T_{MI} \rangle} \geq 0.7$. For all the samples the steady decrease in $\langle \tau \rangle$ for $\frac{T_a}{\langle T_{MI} \rangle} < 0.6$ can be linked to softening of the relaxation barrier on cooling.

The clear drop in $\langle \tau \rangle$ on cooling for all the films below T_{MI} may be considered as one of the most important results. This is because it is opposite to what is expected from a thermal Arrhenius type process controlled by a fixed barrier (U), where $\langle \tau \rangle$ is expected to increase on cooling [$\langle \tau \rangle \sim \exp(\frac{U}{k_B T})$]. However, $\langle \tau \rangle$ can decrease on cooling when the barrier to relaxation is temperature dependent [$U(T)$] and it decreases on cooling as well so that the ratio $\frac{U(T)}{k_B T}$ decreases on cooling. We would discuss later on a physical model to suggest a form for $U(T)$, which will be used for the Monte Carlo simulation.

IV. DISCUSSION

In this section we would try to obtain information on parameters that can control the relaxation process below T_{MI} and thus the process of hysteresis seen with rate cooling/heating as well as the isothermal annealing. We would follow-up with a physical basis for these parameters and would investigate

whether they can be correlated with structural parameters so that the quantitatively different behaviors observed in the three films can have a rationale. Briefly, the tasks in this section can be arranged as follows:

(1) To propose physical model that can be used for the Monte Carlo simulation.

(2) To simulate the hysteresis curves for the three films obtained under constant rate cooling and heating and obtain the physical parameters of the model as proposed in for the three films.

(3) Using the same physical parameters as above carry out the simulation of isothermal annealing.

(4) Investigate any correlation of the parameters so obtained in (2) to the structural parameters as measured in the three films.

A. The physical model and relaxation process

A phase transformation would involve relaxation through a barrier (U) and in most common cases would involve a Arrhenius type relation [30],

$$\tau(T) = \tau_0 \exp\left(\frac{U}{k_B T}\right), \quad (5)$$

where $\tau(T)$ is relaxation time at temperature T . As discussed before, our observation is that the T dependence of $\tau(T)$ is contrary to what is expected for relaxation through a fixed U . A temperature-dependent U , that decreases on cooling, is needed to make $\tau(T)$ decrease with temperature. Given the fact that we may have a distribution of activation energy we use a modified stretched Arrhenius form (with $\alpha < 1$) that allows for a hierarchy in distribution as shown below:

$$\begin{aligned} \langle \tau(T) \rangle &= \tau_0 \exp\left(\left(\frac{U(T)}{k_B T}\right)^\alpha\right) \\ &= \tau_0 \exp\left(\left(\frac{E^*}{k_B}\right)^\alpha \left(\frac{T - T^*}{T}\right)^\alpha\right), \end{aligned} \quad (6)$$

where $\langle \tau \rangle$ is an average relaxation time. The temperature-dependent barrier was assumed to have a simple form [31]

$$U(T) = E^*(T - T^*). \quad (7)$$

E^* is scale for the transformation energy and has the dimension of energy/temperature. We have used E^* and T^* as fit parameters in the simulation. Additionally, the parameter can depend on T as well as on the ramp rate $\frac{dT}{dt}$ for heating and cooling.

The temperature T^* needs mention. It is an empirical parameter. This is needed to make the barrier $U \rightarrow 0$ at a finite nonzero temperature so that the ratio $\frac{U(T)}{k_B T}$ does not blowup as $T \rightarrow 0$. Later on we would seek more physical basis for T^* .

B. The Monte Carlo simulation

The Monte Carlo simulation has been carried out using Eqs. (6) and (7) with fit parameters E^* and T^* , which fix the potential barrier $U(T)$. Details of the simulation procedure are given in the SM [26]. Here we present a gist. The probability p for transformation is $\propto \langle \tau \rangle^{-1}$. For the rate heating and cooling

experiment, it is given by the following relation:

$$p(T) = \exp\left(-\left(\frac{E^*}{k_B}\right)^\alpha \left(\frac{T - T^*}{T}\right)^\alpha\right) \times \gamma \quad (8)$$

where the constant γ is a constant that normalizes the probability and also encompasses prefactor τ_0^{-1} .

For the isothermal annealing since the temperature is held constant at T_a , the probability p also becomes time dependent that would tag-on with the relaxation process. We use the following relation for the time-dependent $p(t)$ where a stretched exponential has been added as the time-dependent part,

$$\begin{aligned} p(t, T = T_a) &= \exp\left(-\left(\frac{E^*}{k_B}\right)^\alpha \left(\frac{T - T^*}{T}\right)^\alpha\right) \\ &\times \gamma \times \exp\left(-\left(\frac{t - t_0}{\tau}\right)^\beta\right). \end{aligned} \quad (9)$$

t_0 is the start time of the anneal process at $T = T_a$.

The simulation that follows the transformation and change in the volume of the metastable metallic state gives us the change in the insulating volume fraction. The n is density of transforming regions (TRs), which is both time (t) and temperature (T) dependent. The transformation of the high-temperature phase to the low-temperature insulating phase will reduce n and the insulating volume fraction. The simulation obtains the insulating volume fraction given as

$$\zeta_v(t, T) = \frac{n_{\max} - n(t, T)}{n_{\max}}. \quad (10)$$

The n_{\max} is the initial value of TR density, which decreases on cooling or on isothermal annealing below T_M . This information was then used to calculate the resistivity $\rho_{\text{cal}}(T)$ for rate heating and cooling experiment and $\rho_{\text{cal}}(T = T_a, t)$ for isothermal annealing experiment using an effective medium theory [23,24],

$$\zeta_v = 1 - \frac{\rho_M(\rho_{\text{cal}} - \rho_I)}{\rho_{\text{cal}}(\rho_M - \rho_I)}, \quad (11)$$

where ρ_{cal} , ρ_M , ρ_I are the calculated resistivity and the extrapolated resistivities for metallic and insulating phases respectively. The metallic portion of the resistivity data has been fitted by the equation $\rho_M = \rho_{0M} + \rho_{1M}T$ and extrapolated for the full T range to find out the ρ_M . For the insulating phase we used the variable range hopping equation

$$\rho_I T^{-1/4} = \rho_{0I} \exp[T_0^{1/4} T^{-1/4}]. \quad (12)$$

Conversely, one can also obtain ζ_v from the Eq. (11), using the observed resistivity data ρ_{obs} , in place of ρ_{cal} .

The details of the parameters, which are used in the simulation are given in Table III. The simulation has been iterated till best matches are obtained between the insulating volume fraction obtained experimentally from the observed resistivity data ρ_{obs} and that obtained from the simulation. The resistivity data then have been reconstructed using the insulating volume fraction obtained from simulation using Eq. (11) and compared with the experiment. In Fig. 7, we have shown the experimental resistivity (as a function of $\frac{1}{T}$) along with calculated resistivity data as obtained from simulation for few representative ramp rates. Good match has been obtained with the data for all the ramp rates in the three films.

TABLE III. Simulation details.

Sample	$T_{MI,C}$	T^*	$\frac{T^*}{\langle T_{MI} \rangle}$	n_{\max} ($1/\mu\text{m}^3$)	E^* (meV/K)	α	ζ_v (T_{MI}) from Eq. (11)
NNO/LAO	105	30	0.22	4×10^6	3.54	0.33	0.109
NNO/BTO/STO	124	50	0.34	4.2×10^5	43.13	0.29	0.196
NNO/STO	191	90	0.45	5×10^4	86.25	0.25	0.012

$T_{MI,C}$ experimental data at ramp 5 K/min, E^* at ramp 5 K/min and α are fit parameters.

The parameters obtained from simulation have been used to calculate the change obtained during isothermal annealing. To compare with isothermal annealing data to the results of the simulation, the following procedure is followed. The variation of the incremental insulating volume fraction ($\Delta\zeta_v$) with time at a given $T = T_a$, [defined as $\Delta\zeta_v(t, T_a) = \zeta_v(t, T_a) - \zeta_v(t = 0, T_a)$] obtained from the simulation has been compared with $\Delta\zeta_v(t, T_a)$ obtained from the experimental annealing data. Variation of both experimental data (points) and the simulation values of $\Delta\zeta_v$ (lines) with time are in Fig. 8 for the three samples at several representative T_a . The match with experimental data is good. Figures 7 and 8 establish the efficacy of the simulation process. The model used a minimal set of physical parameters that can be used to capture the kinetics associated with the relaxation process.

C. Correlation of experimentally observed quantities and simulation parameters with structural parameters

A major quantity obtained from experiment is the average relaxation time ($\langle\tau(T)\rangle$), which decreases monotonously when T is reduced in all the films. Temperature T^* , as defined in Eq. (7), has been introduced to describe the temperature dependence of the barrier to relaxation and such a temperature-dependent barrier has been proposed before in the context of supercooling where T^* has been identified as the limit of supercooling [31,32] even in context of sub- T_{MI} relaxation in NdNiO₃ bulk [22].

The experimental data in the three films can be summarized mainly by four quantities: (a) The transition temperature T_{MI} both during heating and cooling cycle, (b) shift ΔT_{MI} in T_{MI} between the heating and cooling cycles, (c) the scaled height of the hysteresis ξ , and (d) the relaxation time (τ) and its

temperature dependence as observed in isothermal annealing experiments. The simulation presented in the subsections before using a simple model showed that the observed isothermal relaxation as well as the ramp rate-dependent hysteresis can be captured by using essentially two parameters E^* as well as the temperature T^* . In addition, two exponents are needed that describe the stretched nature of the relaxation process, namely α and β , which are both <1 . These parameters have their own characteristics. However, we find that all of them are correlated with two structural parameters, namely, the residual in-plane strain (ϵ_{\parallel}) and/or the average grain (crystallite) size in the film ($\langle d \rangle$) (see Table I). These are shown in Fig. 9. The parameters are dependent on both of them. This clear correlation of the sub- T_{MI} relaxation behavior with structural parameters in NdNiO₃ films is one of the main outcome of the investigation and this has not been observed in past investigations of similar type. Below we explore how the above observations can be rationalized. A complete explanation would need more detailed theories, which, however, is beyond the scope of the present investigation.

A compressive in-plane residual strain in the film stabilizes the high-temperature metallic phase in comparison to the insulating state [18,20]. This shifts the $\langle T_{MI} \rangle$ to lower temperature as can be seen in Table II, where a compressive (tensile) in-plane strain clearly lowers (raises) $\langle T_{MI} \rangle$. The stabilization of the metallic and insulating phases by compressive and tensile strain respectively depend on changes in the free energy [33,34]. It is thus expected that the energy barrier linked parameters like E^* as well as T^* will behave also in the same way as $\langle T_{MI} \rangle$. This can also be seen in Figs. 9(a)–9(c). The ratio $\frac{T^*}{\langle T_{MI} \rangle}$, however, is not constant and lowers progressively when the residual strain becomes more compressive. This can happen if there are other parameters like average

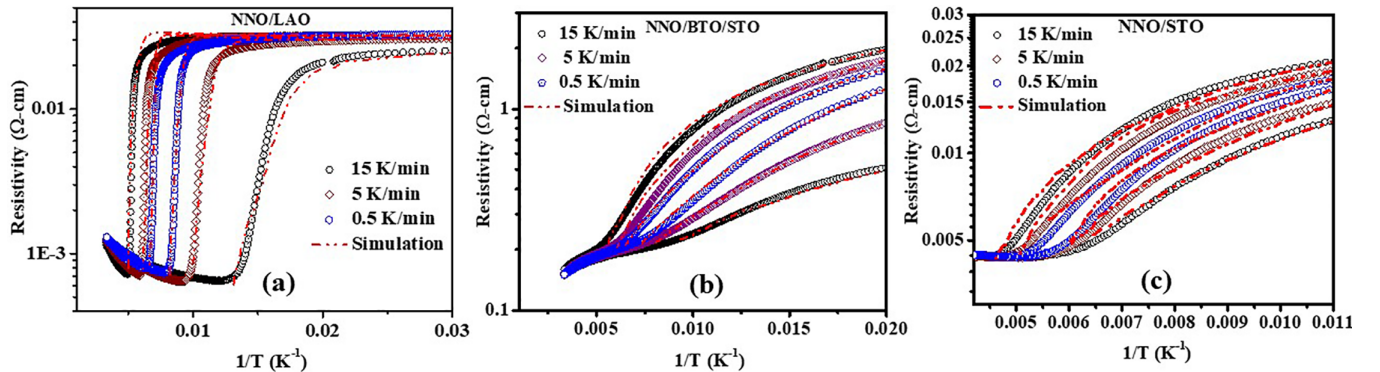


FIG. 7. The ramp rate-dependent hysteresis data (points) for few representative ramp rates along with the simulated data (lines) for (a) NNO/LAO, (b) NNO/BTO/STO, and (c) NNO/STO films. Note the temperature scale in $\frac{1}{T}$, which has been done to accentuate the low- T region.

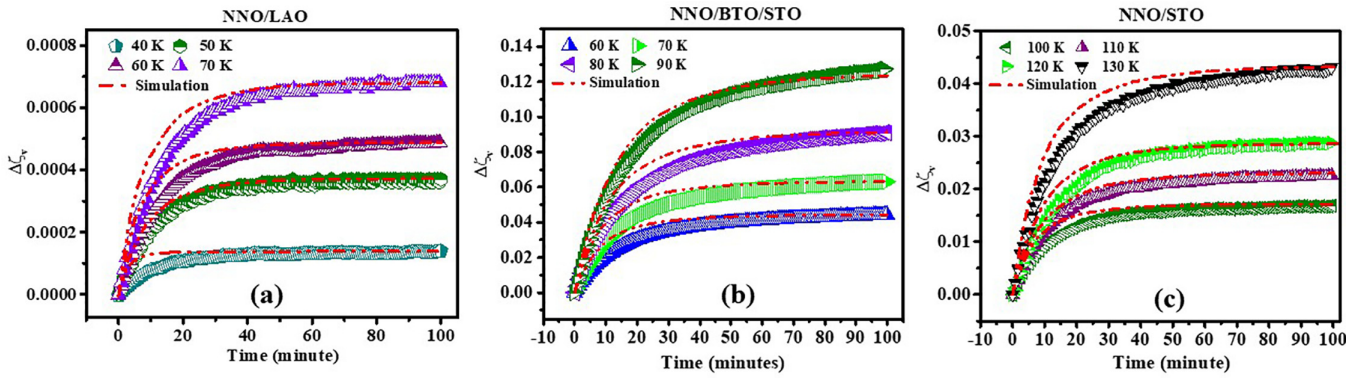


FIG. 8. A comparison of the variation of the insulating volume fraction $\Delta\zeta_v$ with time as obtained from the experiment (points) and from simulation (lines) for (a) NNO/LAO, (b) NNO/BTO/STO, and (c) NNO/STO films at few representative annealing temperatures T_a . The variation of the parameter E^* (as obtained from the simulation) with isothermal annealing temperature for the respective samples are given in supplementary information.

grain size $\langle d \rangle$ that can affect T^* . The process of supercooling is inhibited by presence of heterosurface like a grain boundary. Thus a lower temperature of limit of supercooling is expected in a film that has less heterosurfaces like internal grain boundaries. The coherent grain size being largest in NNO/LAO it can be supercooled to a somewhat lower temperature thus lowering T^* effectively more than what is expected from

larger compressive strain alone. Thus there is an inverse correlation of T^* with $\langle d \rangle$ as shown in Fig. 9(a).

The two observed quantities that have been used to quantify the hysteresis are the width ΔT_{MI} and the normalized height ξ as defined in Eqs. (1) and (3) are given in Figs. 9(e) and 9(f). The width was found to enhance as the strain becomes more compressive although $\langle T_{MI} \rangle$ is reduced when the strain is compressive. The normalized height (which is controlled by the resistivity) was found to enhance as the grain size $\langle d \rangle$ is enhanced. Existence of grains would limit the growth of the correlation length (much like finite size effect) and would affect the growth of the low-temperature phase and the modify the phase transition region. It is also noted that some of the existing models [35,36] relate the hysteresis behavior on distribution the transition temperature in the existing grains that establishing a relation between the hysteresis and the size of crystallographic grains in the system. The sharpness of the transition in the film NNO/LAO that arises from the larger grain size as well as low-quenched disorder makes the height of the hysteresis loop much larger compared to other films.

In Fig. 9(d) we have plotted the dependence of the parameter α as a function of $\langle d \rangle$ and $\epsilon_{||}$. The exponent α that measures degree of non-Debye relaxation has a clear dependence on $\langle d \rangle$. α is smallest in NNO/STO that has the smallest grain size with a higher degree of quenched disorder. In NNO/LAO enhanced grain size and reduced quenched disorder enhances α because the distribution in activation energy is expected to be narrower in such a film.

The parameter E^* defines the scale of energy barrier U . The parameter values obtained from the simulation shows that E^* is dependent on T as well as on the cooling/heating ramp rate. Figure S5 in SM [26] also show in the inset the variation of the parameter E^* with temperature as obtained from the simulation. E^* is lowest as $T \rightarrow T_{MI}$ and it increases monotonically on cooling. This variation is expected as the temperature variation of the barrier will be partly determined by the free energy differences between the two phases. The difference in free energy is lowest at the transition temperature T_{MI} and it increases on cooling as is the case in most phase transitions.

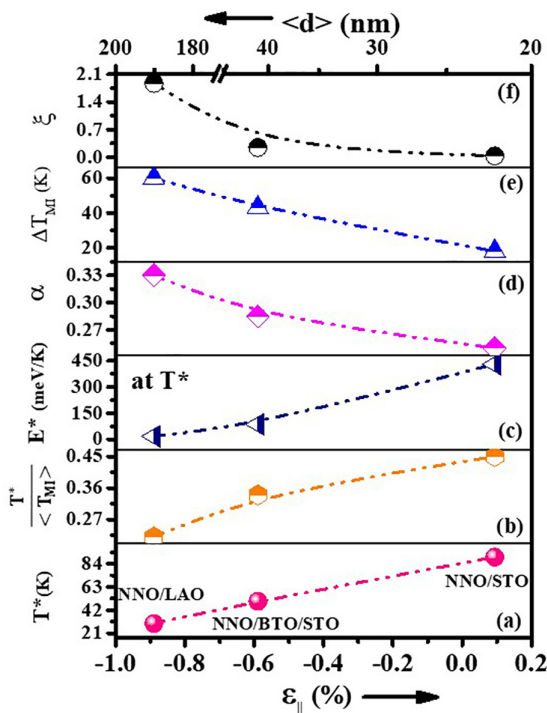


FIG. 9. The variation of simulation parameters (T^* , $\frac{T^*}{\langle T_{MI} \rangle} > E^*$, and α) and observed quantities from hysteretic resistivity curves (ΔT_{MI} and ξ) at ramp 5 K/min with both residual strain ($\epsilon_{||}$) and grain size $\langle d \rangle$. The bottom x axis represents ($\epsilon_{||}$): compressive (left) to tensile (right) indicated by right arrow. The top x axis represents the $\langle d \rangle$, which increases right to left direction indicated by left arrow. The line through the data is guide to the eye.

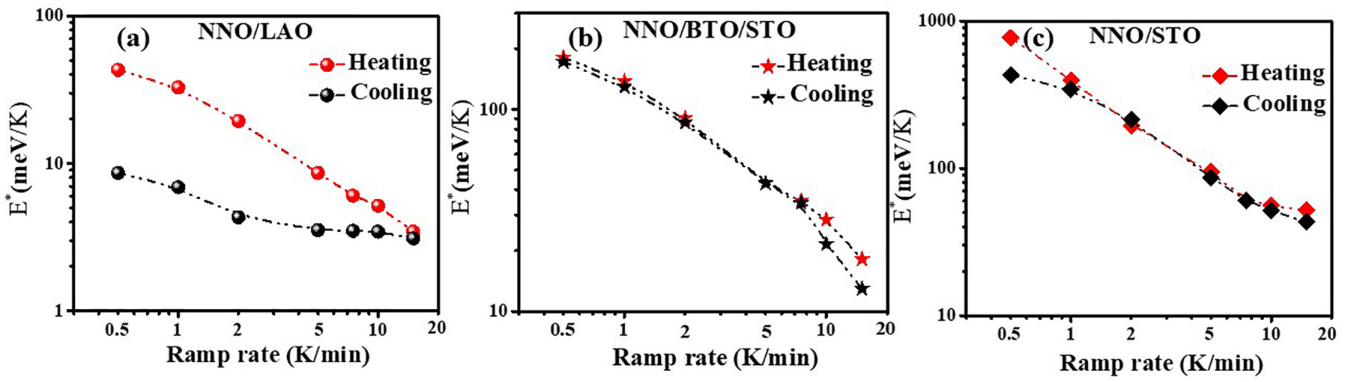


FIG. 10. The variation of E^* with ramp rate for (a) NNO/LAO, (b) NNO/BTO/STO, and (c) NNO/STO.

The variation of E^* with ramp rate (rate of cooling/heating) are plotted in Fig. 10 both for heating and cooling cycles. The E^* has a reciprocal dependence on ramp rate ($\frac{dT}{dt}$). A qualitative explanation can be that at low rate of heating and cooling the two phases between which the transformation occurs can adjust close to their equilibrium free energy value thus enhancing E^* . At a faster rate, the two phases have not adjusted to their equilibrium values and their free energy difference is the lowest giving a low barrier to transformation. The relaxation occurs in a complex energy/potential barrier landscape that depends on T as well as on the ramp rate $\frac{dT}{dt}$ that determines how the phase coexistence evolves. The two-parameter MC model, although it captures the important aspects, does not highlight the complexity associated with such a sub- T_{MI} relaxation. The relaxation occurs where the potential landscape is not spatially uniform and also the stretched exponential coefficient α itself can be both temperature and rate dependent. There is also the issue of local thermodynamic equilibrium between relaxing regions. If these aspects could have been built into the simulation it would certainly improve the model and would make it physically more complete. However, for such a complete model it will be difficult to retain its ease of computation by numerical methods.

An important parameter obtained from the simulation is the density of TR (n) and its temperature dependence. When the sample is cooled or heated at a given rate there is a clear change in n , which in essence controls the relaxation characteristics and the associated hysteresis. A scaled plot of $\frac{n(T)}{n_{\max}}$ vs $\frac{T}{T_{MI}}$ is shown in Fig. 11. n_{\max} is the value of n at $T = T_{MI}$.

The ratio $\frac{n(T)}{n_{\max}}$ decreases monotonously as T is decreased with an approximate exponential dependence on T . The decrease is very similar for the films NNO/STO and NNO/BTO/STO while the temperature dependence is sharper for the film NNO/LAO. This rapid decrease of the ratio $\frac{n(T)}{n_{\max}}$ with T is correlated with the sharp transition seen in the film NNO/LAO as well as the first-order nature with change in symmetry as corroborated by the Raman data.

In this temperature range $T \rightarrow T^*$, which has been proposed as the limit of stability of the high-temperature metallic phase, $\frac{n(T)}{n_{\max}}$ shows a rapid decrease.

In the context of magnetic transition, in particular in materials like perovskite oxides, there are extensive investigations of slow dynamics resulting from relaxation in supercooled

high-temperature metastable phase using temperature and magnetic field as tuning parameter. A glass like kinetically frozen phase [37] in the metastable region had been observed. The slow relaxation arising below the T_{MI} , which has been investigated here, however, have a qualitative difference that there is no kinetically arrested phase as the average relaxation time becomes shorter on cooling.

D. Phase co existence and Raman spectroscopy data

The data on relaxation of resistivity as well as hysteresis at a fixed cooling and heating rate have been analyzed with MC based on a phenomenological model, which uses phase coexistence below T_{MI} . Although such analysis captures the important observations, it will be interesting to investigate, whether data obtained from Raman spectroscopy can throw new light on the nature of the coexisting phases. This subsection explores this aspect albeit qualitatively.

There is clear evidence from Raman spectra for the line at around 300 cm^{-1} that the high- T orthorhombic metallic phase with $Pbnm$ symmetry coexist with the low-temperature monoclinic phase with $P2_{1/n}$ symmetry. This can be seen in Fig. 2. The modes near 300 cm^{-1} arise from antiphase rotation the corner sharing NiO_6 octahedra. The distortion in the octahedra in the low-temperature phase arises from charge

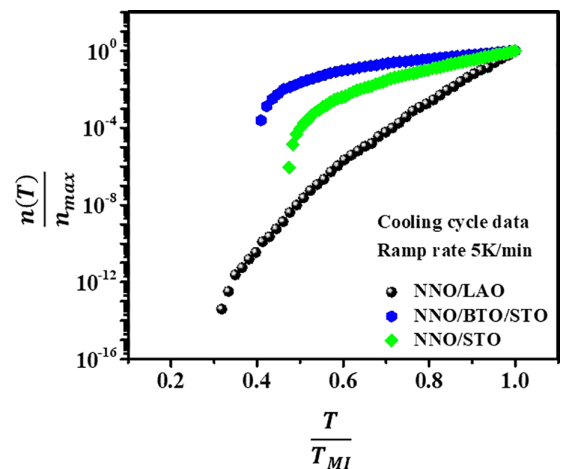


FIG. 11. Scaled variation of TR density (n) with uniform scaled cooling at 5 K/min for the samples.

disproportionation leading to deviation from uniform valency of Ni^{3+} in the high-temperature phase. Thus the phase coexistence can be inferred as coexistence of two types of Ni valency and/or bond disproportionation [38]. Phase coexistence and hysteresis in Raman spectroscopy data have been observed before as well [8,16].

There is a finite barrier to the transformation of two phases that is temperature dependent and makes the phase transformation slow although the relaxation rate increases considerably on cooling. The barrier is likely to have structural origin although coupled electron-phonon mechanisms can also be a possibility as has been proposed in recent investigations [39].

In the following we suggest a likely microscopic scenario for the sample dependence of the parameters E^* and T^* . The metal-insulator transition involves change in the symmetry as established by the XRD data as well as the Raman spectroscopy data. The phase separation leads to local symmetry breaking leading to first-order transition. The phase separation also has a nanoscopic aspect to it as has been observed by photoemission electron microscopy (PEEM) [40]. The PEEM imaging shows that the coexisting phase fractions evolve as one traverses the hysteretic path around T_{MI} . This has been evaluated quantitatively by the MC simulation in the present investigation (see Fig. 8).

It has been stated before that the phase coexistence below T_{MI} would involve coexistence of two phases, one with Ni valency 3^+ uniform within the high-temperature metallic phase with essentially undistorted NiO_6 octahedra and other (majority phase) with charge and bond disproportionation, in distorted octahedron. The barrier to phase transformation would thus largely be decided by the energetics of the transformation of the undistorted octahedron to a distorted octahedron. The strain plays an additional role in tuning the extent of distortion in the octahedra. The occupancy of the crystal field split orbitals also changes with this distortion. For instance, measurement of resonant inelastic x-ray scattering as shown that NNO/LAO has degenerate e_g levels while tensile strain in NNO/STO splits the e_g levels [41]. The dependence of various experimental parameters as well as those obtained from the simulation on the residual strain primarily depend on this factor. For instance, in NNO/LAO film the compressive nature of the film reduces the distortion of the NiO_6 octahedra in the insulating phase. This reduces the barrier to the phase transformation (E). On the other hand for NNO/STO with large tensile strain the barrier is the largest.

The temperature T^* , which is linked to limit of supercooling will be determined largely by the free energy difference between the coexisting phases as well as by the density of nucleating sites. For NNO/STO, presence of larger density of grain boundaries promote more nucleating sites. It has also been reported recently that tensile strain (as it happens in NNO/STO) also promotes creation of oxygen vacancy centres [42], which will also add to creation of new nucleating centres. This will reduce the extent of supercooling region and would enhance T^* . On the other hand for NNO/LAO the distortion of the NiO_6 being least the free energy difference of the two

coexisting phases will be least and also it has larger grain size leading to lower density of nucleating sites. This would thus allow supercooling down to lower temperature making T^* the lowest of the three films.

V. CONCLUSIONS

In this investigation we have extensively studied the slow kinetics of relaxation and its temperature dependence below the metal-insulator (MI) transition temperature T_{MI} that happen in NdNiO_3 thin films grown on three different substrates. The MI transition in such films have coexisting phases and for $T < T_{MI}$ the metastable high-temperature metallic phase that has its persistence in the stable low-temperature insulating matrix transforms into stable insulating phase over cooling. The kinetics have been investigated by two sets of experiments. First, a ramp rate-dependent hysteresis in the resistivity that arise during thermal cycling above and below the T_{MI} and the other with isothermal annealing below T_{MI} at a fixed temperature T_a . One important observation from the isothermal annealing experiment is that the average relaxation time $\langle \tau \rangle$ decreases on cooling, contrary to the expectation of relaxation through a fixed barrier. This led us to propose a temperature-dependent barrier to relaxation that leads to a relaxation time decreasing on cooling. This led to introduction of a temperature T^* in the temperature dependence of the barrier, which has been interpreted as a likely limit of supercooling.

The resistance relaxation data were accompanied by extensive XRD as well as Raman spectroscopy data that confirm the underlying phase transition (with symmetry change) as well as the role of residual strain in determination of parameters that control the relaxation process.

The kinetic experiments were analyzed by Monte Carlo simulation based on a minimal set of parameters, namely, a temperature T^* where the relaxation time $\rightarrow 0$ and an energy scale of transformation E^* . The parameters used in the simulation and also the experimental quantities like the MI transition temperature T_{MI} , the width of hysteresis and the height of hysteresis were found to be correlated with certain structural parameters like the residual strain the film as well as the crystallite grain size that determine the size range in these films. Plausible rationalization of the observations have been suggested.

ACKNOWLEDGMENTS

A.K.R. acknowledges Science and Engineering Research Board (SERB) Projects EMR/2016/002855/PHY and SB/DF/008/2019 for financial support. P.M. thanks Mr. Anirban Goswami for his suggestions related sample preparation. S.S. acknowledges SERB for Projects ECR/2016/001376 and CRG/2019/002668. A.S. acknowledges CSIR for fellowship [File No. 09/1020(0209)/2020-EMR-I]. Authors acknowledge equipment facilitation support from Technical Cell ad Technical Research Centre at S. N. Bose National Centre for Basic Sciences.

- [1] D. B. McWhan, A. Menth, J. P. Remeika, F. Brinkman, and T. M. Rice, *Phys. Rev. B* **7**, 1920 (1973).
- [2] H.-T. Kim, Y. W. Lee, B.-J. Kim, B.-G. Chae, S. J. Yun, K.-Y. Kang, K.-J. Han, K.-J. Yee, and Y.-S. Lim, *Phys. Rev. Lett.* **97**, 266401 (2006).
- [3] G. Catalan, *Phase Transit.* **81**, 729 (2008).
- [4] S. Catalano, M. Gibert, J. Fowlie, J. Íñiguez, J.-M. Triscone, and J. Kreisel, *Rep. Prog. Phys.* **81**, 046501 (2018).
- [5] S. Middey, J. Chakhalian, P. Mahadevan, J. W. Freeland, A. J. Millis, and D. D. Sarma, *Annu. Rev. Mater. Res.* **46**, 305 (2016).
- [6] X. Granados, J. Fontcuberta, X. Obradors, and J. B. Torrance, *Phys. Rev. B* **46**, 15683 (1992).
- [7] V. Scagnoli, U. Staub, M. Janousch, A. M. Mulders, M. Shi, G. I. Meijer, S. Rosenkranz, S. B. Wilkins, L. Paolasini, J. Karpinski, S. M. Kazakov, and S. W. Lovesey, *Phys. Rev. B* **72**, 155111 (2005).
- [8] I. Ardizzone, J. Teyssier, I. Crassee, A. B. Kuzmenko, D. G. Mazzone, D. J. Gawryluk, M. Medarde, and D. van der Marel, *Phys. Rev. Res.* **3**, 033007 (2021).
- [9] D. Li, K. Lee, B. Y. Wang, M. Osada, S. Crossley, H. R. Lee, Y. Cui, Y. Hikita, and H. Y. Hwang, *Nature (London)* **572**, 624 (2019).
- [10] S. Johnston, A. Mukherjee, I. Elfimov, M. Berciu, and G. A. Sawatzky, *Phys. Rev. Lett.* **112**, 106404 (2014).
- [11] R. S. Bisht, S. Samanta, and A. K. Raychaudhuri, *Phys. Rev. B* **95**, 115147 (2017).
- [12] A. S. McLeod, E. van Heumen, J. G. Ramirez, S. Wang, T. Saerbeck, S. Guenon, M. Goldflam, L. Andereg P. Kelly, A. Mueller *et al.*, *Nat. Phys.* **13**, 80 (2017).
- [13] M. M. Qazilbash, A. Tripathi, A. A. Schafgans, B. J. Kim, H. T. Kim, Z. Cai, M. V. Holt, J. M. Maser, F. Keilmann, O. G. Shpyrko, and D. N. Basov, *Phys. Rev. B* **83**, 165108 (2011).
- [14] K. W. Post, A. S. McLeod, M. Hepting, M. Bluschke, Y. Wang, G. Cristiani, G. Logvenov, A. Charnukha, G. X. Ni, P. Radhakrishnan *et al.*, *Nat. Phys.* **14**, 1056 (2018).
- [15] J. A. Alonso, M. J. Martínez-Lope, M. T. Casais, J. L. García-Muñoz, and M. T. Fernández-Díaz, *Phys. Rev. B* **61**, 1756 (2000).
- [16] M. Zaghrioui, A. Bulou, P. Lacorre, and P. Laffez, *Phys. Rev. B* **64**, 081102(R) (2001).
- [17] C. Girardot, J. Kreisel, S. Pignard, N. Caillault, and F. Weiss, *Phys. Rev. B* **78**, 104101 (2008).
- [18] S. Chatterjee, R. S. Bisht, V. R. Reddy, and A. K. Raychaudhuri, *Phys. Rev. B* **104**, 155101 (2021).
- [19] R. Yamamoto, T. Furukawa, K. Miyagawa, T. Sasaki, K. Kanoda, and T. Itou, *Phys. Rev. Lett.* **124**, 046404 (2020).
- [20] P. Majhi, S. Chatterjee, R. S. Bisht, V. R. Reddy, B. Ghosh, and A. K. Raychaudhuri, *Phys. Rev. Mater.* **5**, 085005 (2021).
- [21] C. Yang, Y. Wang, D. Putzky, W. Sigle, H. Wang, R. A. Ortiz, G. Logvenov, E. Benckiser, B. Keimer, and P. A. van Aken, *Symmetry* **14**, 464 (2022).
- [22] D. Kumar, K. P. Rajeev, J. A. Alonso, and M. J. Martínez-Lope, *J. Phys.: Condens. Matter* **21**, 185402 (2009).
- [23] D. S. McLachlan, *J. Phys. C: Solid State Phys.* **20**, 865 (1987).
- [24] K. H. Kim, M. Uehara, C. Hess, P. A. Sharma, and S.-W. Cheong, *Phys. Rev. Lett.* **84**, 2961 (2000).
- [25] B. Poojitha, A. Rathore, A. Kumar, and S. Saha, *Phys. Rev. B* **102**, 134436 (2020).
- [26] See Supplemental Material at <http://link.aps.org/supplemental/10.1103/PhysRevB.108.064103> for fitted parameters of kinetics data, RSM data, XRD data, M-C simulation details.
- [27] J. L. García-Muñoz, M. A. G. Aranda, J. A. Alonso, and M. J. Martínez-Lope, *Phys. Rev. B* **79**, 134432 (2009).
- [28] E. Artin, *The gamma function*, Holt, Rinehart, and Winston (1964).
- [29] A. S. Keys, J. P. Garrahanc, and D. Chandler, *Proc. Natl. Acad. Sci. USA* **110**, 4482 (2013).
- [30] K. J. Laidler, *Chemical Kinetics*, 3rd ed. (Harper & Row, New York, 1987) p. 42.
- [31] P. M. Chaikin and T. C. Lubensky, *Principles of Condensed Matter Physics* (Cambridge University Press, Cambridge, 2000).
- [32] P. Chaddah and S. B. Roy, *Phys. Rev. B* **60**, 11926 (1999).
- [33] A. J. Hauser, E. Mikheev, N. E. Moreno, J. Hwang, J. Y. Zhang, and S. Stemmer, *Appl. Phys. Lett.* **106**, 092104 (2015).
- [34] L. Wang, K. A. Stoerzinger, L. Chang, X. Yin, Y. Li, C. S. Tang, E. Jia, M. E. Bowden, Z. Yang, A. Abdelsamie *et al.*, *ACS Appl. Mater. Interfaces* **11**, 12941 (2019).
- [35] F. Preisach, *Z. Phys.* **94**, 277 (1935).
- [36] J. G. Ramírez, A. Sharoni, Y. Dubi, M. E. Gómez, and I. K. Schuller, *Phys. Rev. B* **79**, 235110 (2009).
- [37] K. Kumar, A. K. Pramanik, A. Banerjee, P. Chaddah, S. B. Roy, S. Park, C. L. Zhang, and S. W. Cheong, *Phys. Rev. B* **73**, 184435 (2006).
- [38] R. J. Green, M. W. Haverkort, and G. A. Sawatzky, *Phys. Rev. B* **94**, 195127 (2016).
- [39] S. Fomichev, G. Khaliullin, and M. Berciu, *Phys. Rev. B* **101**, 024402 (2020).
- [40] G. Mattoni, P. Zubko, F. Maccherozzi, A. J. H. van der Torren, D. B. Boltje, M. Hadjimichael, N. Manca, S. Catalano, M. Gibert, Y. Liu *et al.*, *Nat. Commun.* **7**, 13141 (2016).
- [41] M. H. Upton, Y. Choi, H. Park, J. Liu, D. Meyers, J. Chakhalian, S. Middey, J.-W. Kim, and P. J. Ryan, *Phys. Rev. Lett.* **115**, 036401 (2015).
- [42] L. Wang, S. Ju, L. You, Y. Qi, Y.-W. Guo, P. Ren, Y. Zhou, and J. Wang, *Sci. Rep.* **5**, 18707 (2015).